Applied Energy 359 (2024) 122720

Contents lists available at ScienceDirect

Applied Energy

journal homepage: www.elsevier.com/locate/apenergy

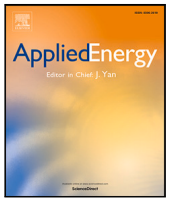

City-scale solar PV potential estimation on 3D buildings using multi-source RS data: A case study in Wuhan, China

Zhe Chen [a], Bisheng Yang [a,*], Rui Zhu [b], Zhen Dong [a]

[a] State Key Laboratory of Information Engineering in Surveying, Mapping and Remote Sensing, Wuhan University, Wuhan 430079, China
[b] Institute of High Performance Computing (IHPC), Agency for Science, Technology and Research (A*STAR), 1 Fusionopolis Way, Singapore 138632, Republic of Singapore

ARTICLE INFO

Keywords:
Sustainable development goals
Multi-source remote sensing data
Building solar photovoltaic potential
Deep learning
Unsupervised domain adaptation

ABSTRACT

Assessing the solar photovoltaic (PV) potential on buildings is essential for environmental protection and sustainable development. However, currently, the high costs of data acquisition and labor required to obtain 3D building models limit the scalability of such estimations extending to a large scale. To overcome the limitations, this study proposes a method of using freely available multi-source Remote Sensing (RS) data to estimate the solar PV potential on buildings at the city scale without any labeling. Firstly, Unsupervised Domain Adaptation (UDA) is introduced to transfer the building extraction knowledge learned by Deep Semantic Segmentation Networks (DSSN) from public datasets to available satellite images in a label-free manner. In addition, the coarse-grained land cover product is utilized to provide prior knowledge for reducing negative transfer. Secondly, the building heights are derived from the global open Digital Surface Model (DSM) using morphological operations. The building information obtained from the above two aspects supports the subsequent estimation. In the case study of Wuhan, China, the solar PV potential on all buildings throughout the city is estimated without any data acquisition cost or human labeling cost through the proposed method. In 2021, the estimated solar irradiation received by buildings in Wuhan is 289737.58 GWh. Taking into account the current technical conditions, the corresponding solar PV potential is 43460.64 GWh, which can meet the electricity demands of residents. The code and test data for building information extraction are available at https://github.com/WHU-USI3DV/3DBIE-SolarPV.

1. Introduction

For a long time in the past, the energy required for urban construction and economic development heavily depended on fossil fuels, resulting in problems of environmental pollution [1]. After the Paris Agreement, which sets a target of reducing net anthropogenic greenhouse gas emissions in the latter half of the 21st century [2], the clean energy industry is booming, with solar photovoltaic (PV) industry experiencing significant growth [3,4].

In China, as a response to the sustainable development and dual carbon goals, the cumulative installed capacity has reached 250 GW by the end of 2020 [5]. There is a concerted effort to not only construct concentrated solar power stations but also to vigorously promote distributed solar PV within urban areas, especially building-integrated photovoltaics (BiPVs). This is mainly due to the fact that buildings are ideal locations for the placement of solar PV modules [6], overcoming the limitations of high land rent and unavailability [7,8]. Besides, buildings are the main source of city energy consumption. BiPV-generated electricity can be directly applied to buildings, reducing transmission losses and contributing to net-zero energy buildings [9,10]. However, due to factors such as location, shading, and energy demand, not every building is appropriate for installing solar PV modules [11]. Thus, it is indispensable to estimate the solar PV potential on buildings for planning installations.

Some scholars directly use publicly available building data or statistics to estimate [12–14]. Nevertheless, the data employed by these methods are usually outdated and unavailable for most regions, which limits their application [15]. Therefore, studies have focused on how to obtain building information for solar PV potential estimation. Some studies use Light Detection and Ranging (LiDAR) data or stereo photos to obtain accurate 3D models [16,17]. These methods can describe the precise 3D form of buildings and even the rooftop geometry [18]. But such data are expensive to obtain, limiting their application on a city-wide scale. In contrast, the Remote Sensing (RS) image is relatively cost-effective, and it is widely used in building extraction for solar

* Corresponding author.
E-mail address: bshyang@whu.edu.cn (B. Yang).

https://doi.org/10.1016/j.apenergy.2024.122720
Received 25 May 2023; Received in revised form 25 November 2023; Accepted 21 January 2024
Available online 1 February 2024

potential estimation [19,20]. These methods usually obtain the building footprints through deep learning but neglect detailed 3D information such as height. Yan et al. [21] proposed a detail-oriented method for constructing 3D building models from optical RS images. However, deep learning, as a data-driven approach [22], requires lots of data with labels, restricting its scalability. Zhong et al. [11] designed a sampling strategy to reduce the required labels and estimated solar PV potential using open Google Earth Satellite (GES) images. However, this approach still requires manual labeling. The limitations of current methods can be summarized as follows based on the above analysis: (1) High-precision data is constrained by cost and challenging to promote. (2) Low-cost data is limited in accuracy, making it difficult to obtain 3D information. (3) Due to data heterogeneity, the generalization ability of deep learning methods is relatively weak. In summary, due to the limitations of data or labeling costs, it is still challenging to assess the solar PV potential at the city scale from a 3D perspective.

To solve the problem, this study proposes a framework based on multi-source RS data that are publicly available, extracting 3D building information in a label-free manner to conduct a city-scale solar PV potential estimation. This study's primary contributions are listed as follows:

(1) The 3D building information is obtained without any data or label costs. Specifically, building footprints are extracted through Unsupervised Domain Adaptation (UDA) with a prior sample selection strategy which aims to reduce negative transfer, and the building heights are derived from the global open Digital Surface Model (DSM) using morphological operations.
(2) An in-depth analysis of solar PV potential from multiple perspectives is conducted based on the acquired 3D building information. According to the estimated potential, this study considers the perspectives of spatial and temporal distribution, rooftop and facade distribution, and supply and demand balance, providing a basis for planning and decision-making.

2. Related work

2.1. Solar energy potential estimation

Considerable effort has been dedicated to estimating the potential of solar energy on different geographic scales. Several studies utilized social factors for estimation. For instance, solar-applicable rooftop area was estimated throughout Spain based on available data such as building density, population, and land use [23]. The roof area was calculated in the sample region and extrapolated using the roof area-population relationships [12]. These methods are low-cost and can be used for regional policy-making with agglomerate values, but the PV potential is coarse and not well geo-referenced. In a complex urban environment, it is necessary to conduct a more accurate estimation to select suitable places for installing solar PV modules [24]. When geospatial data is available, some researchers use it directly for estimation. Li et al. [13] obtained the building footprints and the digital contour file in the Geographic Information System (GIS) database, and the solar irradiation was mathematically calculated in the pixel cell. Hong et al. [24] acquired building data from government agencies to assess the physical, geographical, and technological potential of solar energy in the Gangnam district of Seoul using hillshade analysis. With the combination of GIS and solar potential estimation models, Assouline et al. [25] evaluated the potential of rooftop PV across the entirety of Switzerland by employing the random forest algorithm. Zhang et al. [26] employed ERA-interim meteorological reanalysis data from the European Centre for Medium-Range Weather Forecasts (ECMWF) to investigate the spatio-temporal distribution of solar energy in China. However, detailed building information for large-scale estimation is rare due to data limitations and rapid urbanization, and some studies acquire building information from RS data for the estimation of solar potential.

2.2. Building information acquisition

As LiDAR can capture 3D information of objects, many studies used this data to accurately estimate the potential of solar PV. For example, Kodysh et al. [27] estimated the solar PV potential of individual rooftops using an upward-looking hemispherical viewshed algorithm [28] with DSM derived from LiDAR. Huang et al. [29] developed a GPU-accelerated model named SHORTWAVE-C which introduced the influence of clouds and estimated the potential using airborne LiDAR. Suomalainen et al. [30] considered the orientation and slope of roofs based on LiDAR to assess the potential on buildings at the regional and urban levels. Liang and Yang [31] calculated the solar potential on building roofs and facades by utilizing ubiquitous point clouds obtained through Unmanned Aerial Vehicles (UAV) and Terrestrial Laser Scanning (TLS). Mohajeri et al. [32] conducted the Support Vector Machine (SVM) with hand-crafted features to classify building roofs into six categories and explored the impact of each category on solar energy potential. Vo et al. [18] utilized airborne LiDAR, directly performing per-point processing based on distributed computing to make full use of all the details provided by the point clouds. Besides, some researchers conducted photogrammetry to obtain building information for estimation. Chen et al. [17] generated DSM from airborne stereo images [33], and developed a quadrant-based segmentation approach to categorize different roof types to better calculate solar energy utilization cost. Some studies discarded the 3D information, directly estimating the solar PV potential from RS images. Li et al. [34] designed a multi-task learning framework to obtain the building footprint and the orientation of each segment of the roof from the Very High Resolution (VHR) images for a more accurate estimation. Notably, Yan et al. [21] suggested a method based on deep learning that constructed 3D building models from VHR satellite images and estimated the potential of solar PV on 3D urban surfaces. However, it is difficult to extend the above methods to other regions due to the limitations of labeled datasets. Thus, open-access data has been explored. Li and Ratti [35] used Google Street View (GSV) panoramas and the building height model to generate hemispherical images, which were combined with the solar path to assess the spatio-temporal solar irradiation distribution in street canyons. Cheng et al. [14] collected building footprints and the corresponding number of floors from OpenStreetMap (OSM) to form the LOD1 model, then discretized the model into a point array and calculated the solar irradiation on the building roof and facade based on points. OSM is a crowd-sourced database, hence there are significant data gaps in many regions, including China, which limited its application. Zhong et al. [11] designed an optimized sampling strategy to produce a training set with less manual labeling costs and utilized deep learning to extract building roofs from GES images. However, this method still requires labeling in the corresponding area, and the trained model cannot be used directly in different regions because of the heterogeneity of GES images. In addition, estimation from 3D perspectives such as occlusion analysis is not possible as only planar information is extracted. Therefore, 3D building information for solar PV potential estimation is difficult to obtain at low human and data costs, which motivates this study.

3. Study area and data collection

3.1. Study area

Wuhan, the capital of Hubei Province and the central city of middle China, is selected as the study area (Fig. 1a). It has a subtropical monsoon climate and significant seasonal variation in solar irradiation. With a permanent population of 13.64 million and a total area of 8569.15 km^2, Wuhan has a large energy consumption demand. Assessing the solar PV potential on buildings within the city is a feasible approach for distributed solar PV farming.

The city comprises 13 districts (Fig. 1b) with varying building styles, making it an ideal sample for testing the effectiveness and scalability of the method.

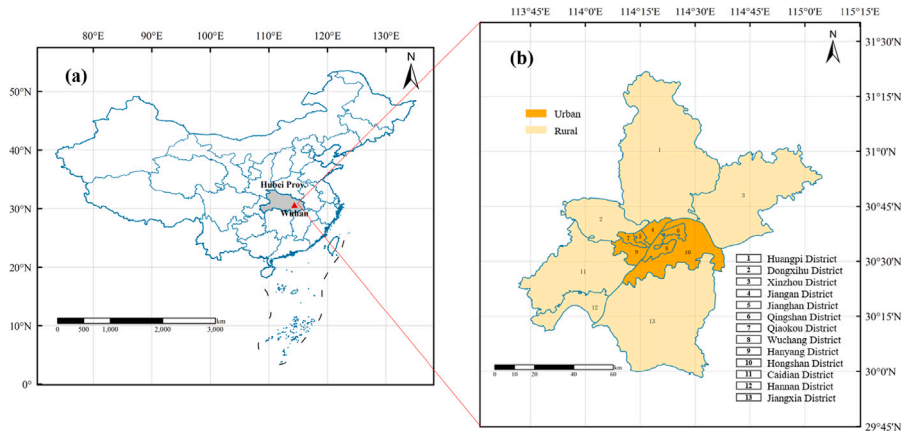

Fig. 1. Study area. (a) The geographic location. (b) Administrative diagram.

3.2. Data collection

The data used comprises GES images, SpaceNet, GlobalLand30, and AW3D30 DSM. Among them, SpaceNet serves as the source domain for UDA, and the knowledge learned from this dataset for building extraction is transferred to GES images. GlobalLand30 is used to provide prior knowledge of land cover to alleviate the domain shift caused by differences in label distribution during the adversarial training. AW3D30 DSM is utilized to provide elevation information to support 3D analysis.

3.2.1. Google earth satellite images

The RS images are collected from the Google Earth platform (https://earth.google.com/), which offers several advantages, including high resolution and wide coverage, making it ideal for large-scale solar PV potential estimation.

The GES images are available in various resolutions with red, green, and blue bands, and cell values range from 0 to 255. In order to extract the buildings accurately, high-resolution images (0.26 m) were downloaded. To ensure the validity of the results, high-quality images from the period between 2019 and 2021 were selected based on the cloudiness and quality of images in each district.

3.2.2. SpaceNet dataset

To extract buildings without additional labeling, UDA semantic segmentation provides a feasible way. This method utilizes a public building dataset as the source domain to transfer knowledge to an unseen target domain. SpaceNet dataset (https://spacenet.ai/datasets/) offers a repository of freely available imagery, which contains about 67,000 km^2 of VHR imagery, more than 11 million building footprints, and about 20,000 km of road labels for research. Building detection dataset [36] provides the need for use in this study, which includes five Areas of Interest (AOI), namely Vegas, Rio, Shanghai, Khartoum, and Paris. Since Shanghai and Wuhan have a similar architectural style and spatial layout, it is appropriate to use SpaceNet-Shanghai as the source domain dataset. The area of SpaceNet-Shanghai is 1000 km^2 and contains 92,015 building footprint polygons, given in the GeoJSON format. To facilitate the training of the UDA network, the labels in GeoJSON format were converted into NumPy format.

3.2.3. GlobalLand30

GlobeLand30 is a global Land Use and Land Cover (LULC) product developed by China with a 30-m spatial resolution [37]. In 2014, the GlobeLand30 2000 and 2010 versions were released. The Ministry of Natural Resources initiated the GlobeLand30 2020 in 2017, which is complete now, and the latest version is utilized in this article. The images employed for GlobeLand30 2020 are primarily 30-m multispectral images, encompassing ETM+, TM5, OLI multispectral images from Landsat, multispectral images from China Environmental Disaster Mitigation Satellite (HJ-1), and 16-m resolution multispectral images from Gaofen-1 (GF-1). GlobeLand30 2020 includes a total of 10 first-level types, namely: artificial surface, cultivated land, grassland, forest land, shrubland, water body, wetland, tundra, bare land, glaciers and permanent snow cover. The data were collected from http://www.globallandcover.com/. A tile covering the city of Wuhan was downloaded and cropped using the Wuhan outline vector, and finally, the artificial surface category was used as a mask.

3.2.4. AW3D30 data

The ALOS World 3D-30 m (AW3D30) dataset is a global DSM with 30 m horizontal resolution (30 arcseconds), which is license-free [38]. It was interpolated from the high-resolution DSM generated by the Panchromatic Remote-sensing Instrument for Stereo Mapping (PRISM), carried on the Advanced Land Observing Satellite (ALOS). Previous works have confirmed that the AW3D30 DSM has higher vertical accuracy than both the Shuttle Radar Topography Mission (SRTM) and the Global Digital Elevation Model (GDEM) [39,40], exhibiting an RMSE of less than 5 m. These properties indicate that AW3D30 DSM is suitable for deriving city-scale building heights. This study utilized the latest version 3.2, and the DSM data for Wuhan was generated from the PRISM data collected in 2014. The data was downloaded from https://www.eorc.jaxa.jp/ALOS/en/aw3d30/data/index.htm, and subsequently cropped using the outline vector of Wuhan.

4. Method

The overall framework for estimating building solar PV potential consists of three parts, as shown in Fig. 2. First, with the help of the public SpaceNet-Shanghai and Globalland30 2020, the building footprints are extracted based on open-source GES images using UDA semantic segmentation. Then, the nDSM of the city is derived by utilizing morphological operations on the AW3D30 DSM. After obtaining the building footprints and heights, shadow occlusion can be considered to assess the potential of solar PV on buildings from a 3D perspective for subsequent analysis.

4.1. Cross-domain building footprint extraction

The Deep Semantic Segmentation Network (DSSN) is biased towards the dataset, so when the trained model is directly applied to other scenes with inconsistent distribution, the performance declines significantly, which is called domain shift [41], as shown in Fig. 3. A certain amount of labeling for new scenes can reduce the domain shift, but it is difficult to extend to a large area as labeling is labor-intensive and time-consuming. To enable the proposed method to be generalized

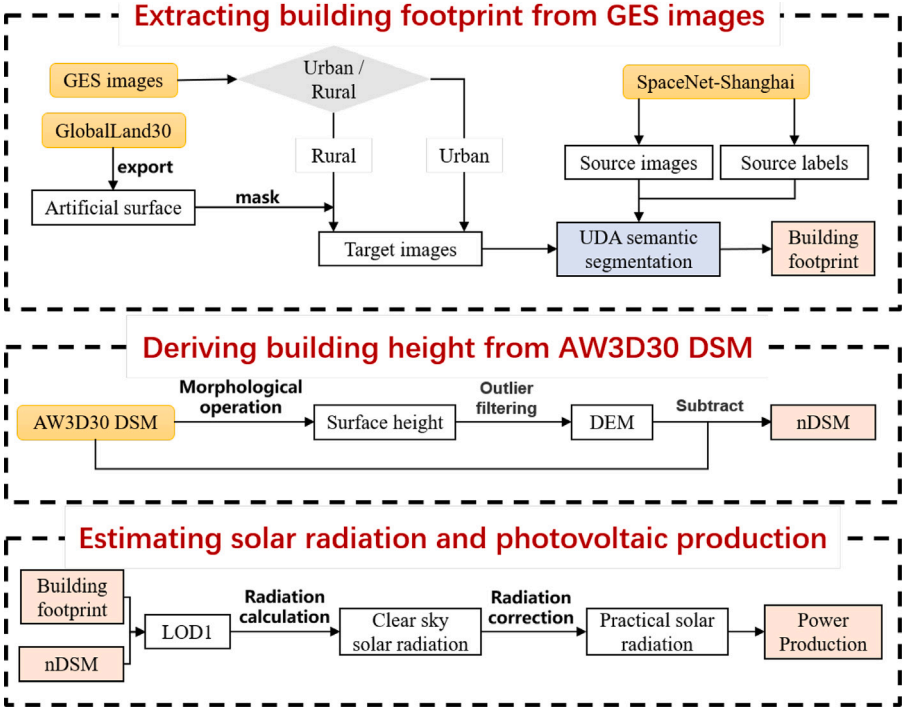

Fig. 2. Framework of solar PV potential estimation on buildings.

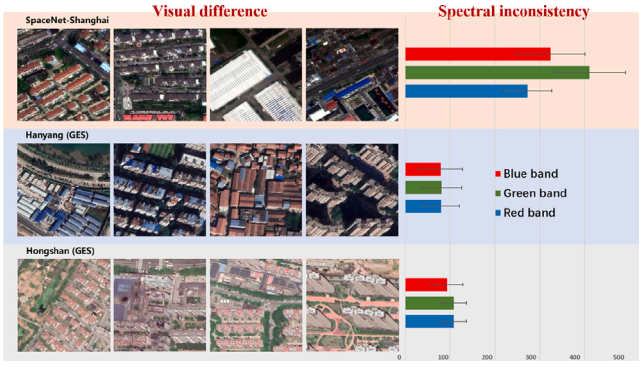

Fig. 3. Visualization difference and spectral inconsistency between datasets.

and applied nationally or globally, UDA is conducted without any additional labeling. This study proposes a method for cross-domain building extraction, as shown in Fig. 4. The labeled SpaceNet-Shanghai dataset is selected as the source domain. The DSSN trained on this dataset is then transferred to the Wuhan GES dataset, which serves as the target domain. Before performing UDA, the downloaded GES images are resized to match the size of the Spacenet-Shanghai dataset, which is 650 × 650, and z-score normalization is employed for the images of both domains.

4.1.1. Label distribution unifying

SpaceNet-Shanghai dataset is a collection of urban area images in Shanghai. Compared with images in the rural area, although the landcover categories are the same, there is an inconsistency between urban and rural in label distribution [42]. One common approach to address this issue is self-training, which involves iteratively generating pseudo-labels for the target data and using them to retrain the network [43–45]. However, when the domain shift is significant, it becomes challenging to generate sufficient accurate pseudo-labels to guide the training. Conducting adversarial training to diminish domain shift before self-training can improve overall performance.

Unlike street-view images, RS images typically have a vertically downward perspective. This identity can facilitate the comprehensive processing of multi-source RS data, even if the data are in different time phases. This study proposes a method for processing raw imagery using the existing coarse-grained LULC product, to ensure a consistent label distribution between urban and rural areas.

As shown in the green area in Fig. 4, when the target area is rural, the Globalland 30 is first indexed according to the category number of artificial surfaces to obtain a mask. The mask is then cropped to the size of the target area using the contours. Finally, the rural GES image is masked to obtain an image with a similar label distribution to the urban area, as shown in the following formula:

$$I_{i,j} = 0 \text{ if } M_{i,j} \neq Ind_{as} \tag{1}$$

Among them, I represents the GES image, M represents the mask, i and j correspond to the row and column of the image, and Ind_{as} is the index of the artificial surface.

Since we only keep the GES images belonging to the artificial surface category, although not very accurate, it guarantees a label distribution close to the source domain, which can greatly reduce the negative transfer when conducting the adversarial domain adaptation.

4.1.2. Alignment in multi-space

Although the gap in label distribution has been eliminated, there is still a domain shift in the image style. To tackle the issue, this study jointly aligns the distribution in both the input space and feature space [46]. Since the resolution of target images is the same as that of source images, the Resolution Uniform (RU) module is removed. As shown in the yellow area in Fig. 4, target images are first processed through Digital Number Transfer (DNT), which can model the mapping relationship of the digital number in the channel dimension. Then multi-level features are extracted from source images and transformed target images, fused by the Multi-Scale Feature Aggregation (MSF), respectively. Finally, the fine-grained discriminator is utilized to discriminate the fused features. The entire network can be partitioned into two components, the segmentation network G and the fine-grained discriminator D, and optimized through a zero-sum game. G is optimized

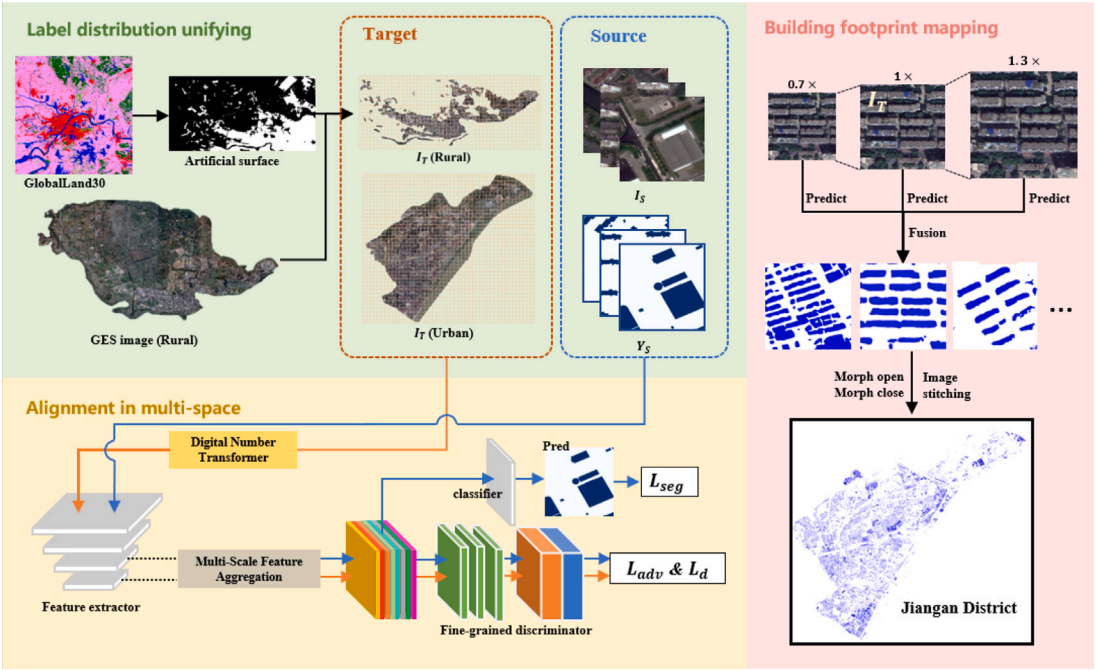

Fig. 4. Framework of cross-domain building footprint extraction.

by solving the following formula with a fixed D:

$$\min_G = \mathcal{L}_{\text{seg}} + \lambda_{\text{adv}}\mathcal{L}_{\text{adv}} \tag{2}$$

The hyperparameter λ_{adv} is used to balance the two losses. The cross-entropy loss L_{seg} is computed using I_s from the source domain and its corresponding label Y_s.

$$\mathcal{L}_{seg} = -\sum_{h,w}\sum_{k} y_s^{(h,w,k)} \log\left(P_s^{(h,w,k)}\right) \tag{3}$$

where $y_s^{(h,w,k)}$ denotes the one-hot label entry for the pixel located at position (h, w) and $P_s^{(h,w,k)}$ refers to the probability predicted by G that the pixel belongs to class k. The following formula presents the adversarial loss L_{adv}:

$$\mathcal{L}_{adv} = -\sum_{h,w}\sum_{k} e_k^{(h,w,1)} \log\left(D\left(P_t\right)^{(h,w,0,k)}\right) \tag{4}$$

To optimize D, L_D is minimized with a fixed G, which is expressed in Eq. (5):

$$\mathcal{L}_D = -\sum_{h,w}\sum_{k} e_k^{(h,w,0)} \log\left(D\left(P_s\right)^{(h,w,0,k)}\right) - \sum_{h,w}\sum_{k} e_k^{(h,w,1)} \log\left(D\left(P_t\right)^{(h,w,1,k)}\right) \tag{5}$$

where e is called domain encodings. For a more detailed introduction of the method, please refer to Chen et al. [46].

4.1.3. Building footprint mapping

The red area in Fig. 4 illustrates the specific process of mapping the building footprints. To adapt to the characteristics of different scales of buildings and further improve the extraction accuracy, Multi-Scale Testing (MST) is used [47,48]. The input image is interpolated to different scales and predicted separately, and then the probability maps at multiple scales are restored to the original size, followed by mean fusion. In addition, morphological opening and closing operations are used to further filter out noisy predictions and fill building holes. Due to memory limitations, a fixed window without overlap is used to perform subregion-by-subregion prediction on the entire GES image, and finally, the building extraction result for the district is obtained. It should be noted that the Globalland 30 is relatively rough, and there are errors in land use, so the mapping is carried out directly on the original GES image, which can ensure that buildings will not be missed due to the erroneous land use.

4.2. Deriving building height from AW3D30 DSM

To estimate and analyze building solar PV potential from a 3D perspective, this study uses AW3D30 DSM as the data source to extract building heights.

Algorithm 1: Building height extraction

Input: AW3D30 DSM D, sliding window size s, image height H, image width W, hyperparameter k
Output: nDSM nD
for $i = 1, 2, ..., H$ **do**
  for $j = 1, 2, ..., W$ **do**
    $window = D(i - s : i + s, j - s : j + s)$
    $window$ = Sort(Flatten($window$))[0: k]
    mean = Mean($window$)
    std = Std($window$)
    foreach n *in window* **do**
      if $|window(n) - mean| > 3 * std$ **then**
        Remove $window(n)$ from $window$
      end
    end
    $DEM(i, j)$ = Mean($window$)
    $DSM(i, j) = D(i, j)$
    $nD(i, j) = DSM(i, j)$ - $DEM(i, j)$
  end
end

Inspired by Huang et al. [49], sliding window operation is conducted to detect surface height and ground elevation, obtaining the DSM and Digital Elevation Model (DEM) of the entire study area. Then, the normalized DSM (nDSM) can be obtained by subtracting the DEM from the DSM, which can indicate the building height. In addition, for noises present in the raw data, outlier detection is used in nDSM

generation to filter them out. Algorithm. 1 presents the flow of the building height extraction method.

The process of calculating ground height (DEM) involves the size of the sliding window s. A larger s makes the area too large, and the calculation result cannot well represent the height of the center point, while a smaller s may cause the window to fall inside a large building, resulting in no ground pixels within the window. s is set to 7 according to experiments in this study. After obtaining the window according to the center pixel, all the pixel values in the window are counted and sorted in ascending order, and the top k smallest values are taken as ground point candidates. In addition, the 3δ criterion is used to detect and remove the outliers in the window. Then, the mean value of the remaining candidate points is calculated as the ground height of the center. Unlike Huang et al. [49], this study does not use the Gaussian kernel for processing, because it will lead to blurred edges of buildings. Different from the processing of ground points, this paper directly uses the height of AW3D30 DSM as surface points, which can preserve the boundaries of buildings. Finally, the nDSM reflecting building height is obtained by subtracting DSM and DEM.

4.3. Estimating solar irradiation and photovoltaic production

Solar irradiation is adjusted when it passes through the atmosphere, further modified by topology and surface features, and finally received by the surface in the form of direct, diffuse, and reflected components. Typically, since the proportion of reflected irradiation is quite minimal, less than 2.4 percent of the total [29], this component is not considered in the calculation and analysis. The calculation of global solar irradiation ($Global_R$) is shown in the following formula:

$$Global_R = Direct_R + Diffuse_R \tag{6}$$

Among them, $Direct_R$ and $Diffuse_R$ quantify the direct and diffuse components of solar irradiation received by the surface objects, respectively.

In this study, the hemispherical viewshed algorithm is employed to estimate the solar irradiation received by roofs, taking into account the mutual shading effects between buildings. Solar irradiation calculations are primarily based on the resulting raster of building heights while building footprint vectors are used to limit the calculation area. For a more detailed description, please refer to Kodysh et al. [27]. To obtain the amount of solar irradiation under the clear sky condition, this study empirically sets the atmospheric transmittance and diffuse ratio as 0.7 and 0.2.

After acquiring the estimated value of solar irradiation under the clear sky condition, conducting further estimations for actual scenarios can more accurately help the decision-making of solar PV module installation. The amount of solar irradiation received by the earth can be significantly impacted by sky clearness conditions (such as sunny, cloudy, or rainy) and atmospheric air turbidity levels (such as pure, normal, or polluted) [50]. Motivated by Cheng et al. [14], this study uses the Ångström-Prescott (Å-P) formula to correct the irradiation, which considers the local weather conditions in the study area. The relationship between sunshine time and solar irradiation is commonly assumed to be linear, and the Å-P formula can describe this relationship as follows:

$$Global_{corr} = Global_R \left(a + b \frac{D_{sun}}{D_{day}} \right) \tag{7}$$

where $Global_{corr}$ is the amount of global solar irradiation corrected by the actual weather conditions, D_{sun} is the daily sunshine duration, which can be obtained from the observation data of the meteorological station, and D_{day} is the daily daytime, which can be calculated based on the latitude of the study area [51]. The coefficients a and b of the Å-P formula can be calculated from the statistical data by linear fitting. In this study, a and b are assigned values of 0.25 and 0.75, respectively, following the previous works [14,52].

Table 1
Quantitative results of building extraction under different settings.

District		Source only	DA only	DA+LU	DA+LU+MST
Wuchang District	IoU	20.07	37.48	65.35	66.76
	F1	33.42	38.11	79.04	80.07
Dongxihu District	IoU	29.62	51.60	60.42	60.64
	F1	45.69	68.07	75.33	75.50

5. Study results

The building footprints, building heights, and solar irradiation distribution results are presented in this section to exhibit the effectiveness of the proposed method.

5.1. Building footprint extraction results

5.1.1. Mask GES images using LULC

According to the spatial layout of urban and rural areas in Wuhan, six of its thirteen districts, including Dongxihu District, Jiangxia District, Caidian District, Huangpi District, Hannan District, and Xinzhou District, are predominantly rural with large expanses of farmland and limited artificial surfaces. In addition, Wuchang District, while urban, features a significant amount of water bodies, resulting in the domain shift between the SpaceNet dataset and the GES images in the label space. Thus, label distribution unifying was applied to these seven districts to bridge the gap in label distribution.

As shown in Fig. 5, the water bodies in Wuchang District were been removed, and a large area belongs to the artificial surface. The other six districts are rural areas with a lot of grassland, forest land, and cultivated land, so a large proportion of the areas were masked out. However, due to the large area of these districts, it is guaranteed that the generated dataset is sufficient for UDA.

5.1.2. Building footprint extraction results

The thumbnail image of the building footprints for the entire Wuhan city is presented in Fig. 6a. The area covered by buildings in Wuhan amounts to 276.7 km^2. The building density decreases gradually from the inside to the outside. This is because the inside districts develop earlier and have a higher degree of urbanization, while the outer districts develop later and the city landscape still belongs to the rural. Fig. 6b further illustrates the phenomenon. The rural district with the blue outline has a lower building density, and the density of buildings near the urban area is relatively high, while the density of the urban districts with the orange outline is higher and the distribution is more uniform. Fig. 6c and d present the more detailed building footprint extraction results in the rural and urban areas, respectively. The proposed building footprint extraction method can achieve excellent performance without any annotation. Since the GES images are not orthorectified, this will affect the extraction results in two ways. On the one hand, buildings will have a certain offset in the image, causing misalignment of footprints and roofs. The offset is more significant in urban districts as the buildings are high-rise, while the GES images in rural districts are close to the orthographic image because numerous buildings are low-rise, so the offset is not obvious. This offset will not affect the cumulative value of building footprints [11]. On the other hand, facades of high-rise buildings will be in the GES image. Building facades and roofs usually share the same material, so the spectral characteristics are similar, which results in difficulty in roof extraction. Building facades are often intrusive under supervised conditions, and even more so under unsupervised conditions. Since this research is an estimation on a large scale, such interference has little impact on subsequent results and recommendations.

To validate the performance of each module in the proposed UDA building footprint extraction method, 50 images in each of the two typical areas were selected for ablation experiments. The F1-Score (F1)

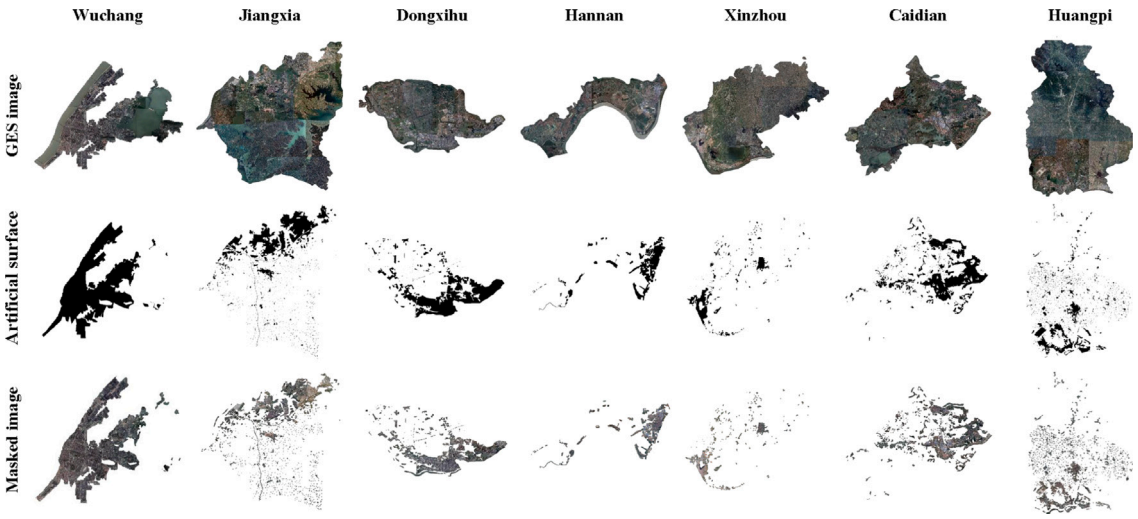

Fig. 5. GES images masked by the impervious surface in LULC.

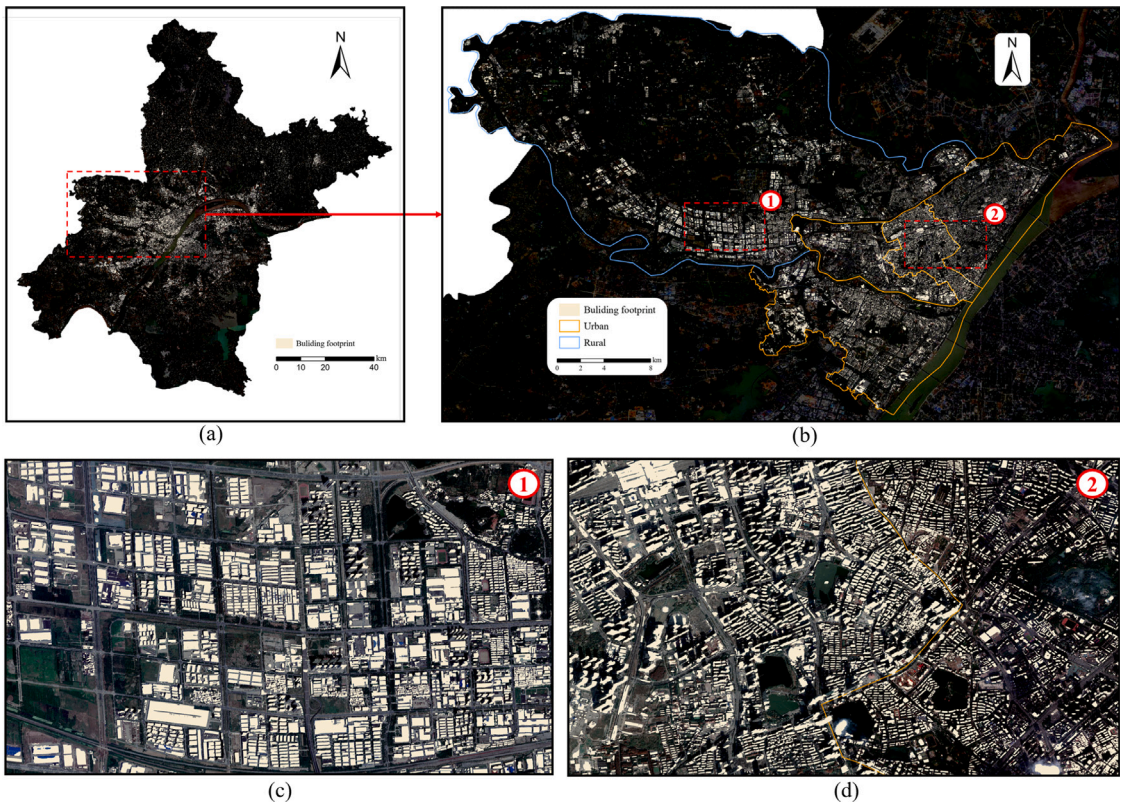

Fig. 6. Cross-domain building extraction results. (a) Extracted building footprints in Wuhan. (b) Extracted building footprints in the selected districts. (c) Detailed building footprints in rural. (d) Detailed building footprints in urban.

and IoU metrics are used for evaluation. The F1-Score, defined in Eq. (8), is calculated based on precision and recall.

$$F1 = \frac{2 \times Precison \times Recall}{Precison + Recall} \tag{8}$$

where

$$Precision = \frac{TP}{TP + FP} \tag{9}$$

$$Recall = \frac{TP}{TP + FN} \tag{10}$$

The IoU is defined as Eq. (11):

$$IoU = \frac{TP}{TP + FP + FN} \tag{11}$$

where TP, FP, and FN indicate the total number of predicted pixels that are true positives, false positives, and false negatives in the test set, respectively.

Table 1 illustrates the quantitative results, and Fig. 7 displays the partial visualization results. Under the source-only setting, the model trained solely on the source domain (SpaceNet-Shanghai) is directly applied to the GES images in Wuhan. Due to the existence of domain shift, the performance is extremely poor, with IoU and F1 below 30% and 46% in two areas. The DA-only method greatly mitigates domain shift as it involves adversarial training to tackle domain shift in both the input and feature space [46]. However, when there is significant variation in LULC, this method can negatively impact the extraction

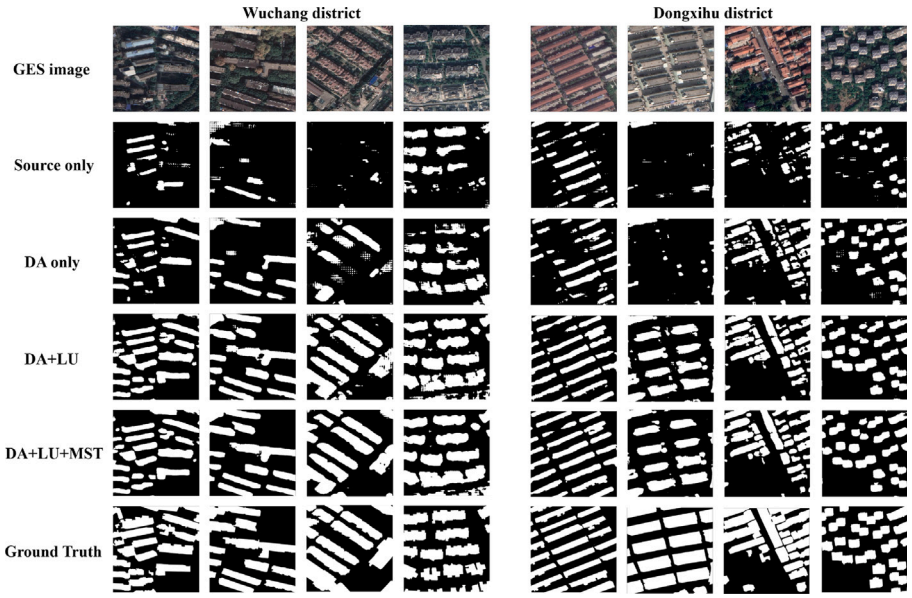

Fig. 7. Visualization results of building extraction under different settings.

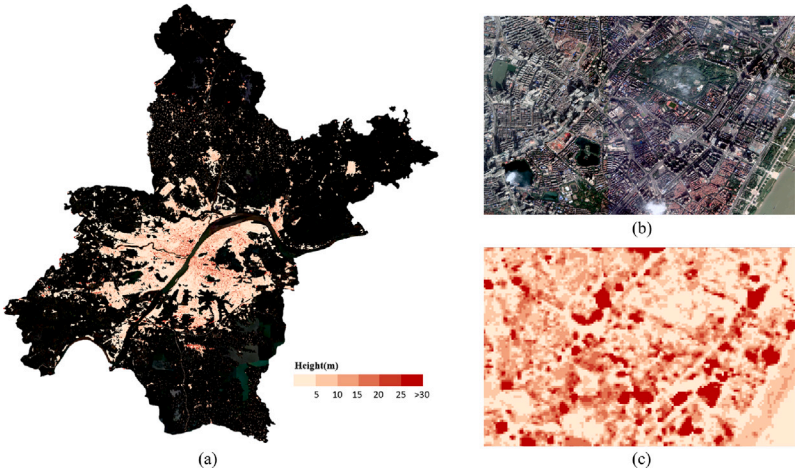

Fig. 8. Building height deriving results. (a) Derived building heights in Wuhan. (b) GES image in the selected area. (c) Building heights in the selected area.

results due to the domain shift in the label space. The LU module proposed in this study can make the LULC, that is, the label space distribution of different domains, tend to be consistent. Therefore, the negative transfer [53] is alleviated, further enhancing the performance of building extraction. With the addition of the LU module, the IoU and F1 increased from 37.48% and 38.11% to 65.35% and 79.04% in Wuchang District, and increased from 51.60% and 68.07% to 60.42% and 75.33% in Dongxihu District, respectively. The MST strategy fully considers the various sizes of buildings and addresses the issue of holes in larger buildings and small extraction errors. Finally, 66.76%, 60.64% IoU and 80.07%, 75.50% F1 were achieved in Wuchang District and Dongxihu District. In summary, the method proposed in this study can effectively obtain building footprints on open GES imagery in an unsupervised manner.

5.2. Building height deriving results

Fig. 8a depicts the building height deriving results for the entire city of Wuhan. This study uses the artificial surface layer of GlobalLand30 to mask the results for better visualization. The results indicate a spatial pattern of decreasing building heights from the urban areas to the rural areas, which is consistent with the building density distribution.

Table 2
Total hours of the D_{sun} and D_{day} in Wuhan in each month of 2021.

Month	D_{sun}	D_{day}	D_{sun}/D_{day}
Jan	129.1	322.4	0.550
Feb	118.5	283.3	0.564
Mar	71.0	371.0	0.394
Apr	59.7	388.0	0.365
May	116.5	424.7	0.456
Jun	147.2	423.5	0.511
Jul	138.0	431.4	0.490
Aug	129.6	410.2	0.487
Sep	226.0	369.5	0.709
Oct	116.1	353.9	0.496
Nov	159.8	318.0	0.627
Dec	161.4	316.2	0.633

One region is selected to show more details about building heights. Due to the rough resolution of the data source used, which is 30 m, it is difficult to accurately obtain the height of a single building. But as can be seen from Fig. 8b, the distribution of buildings, especially in residential areas, has a certain degree of aggregation, that is, the height of buildings is consistent in a certain area. Therefore, the nDSM

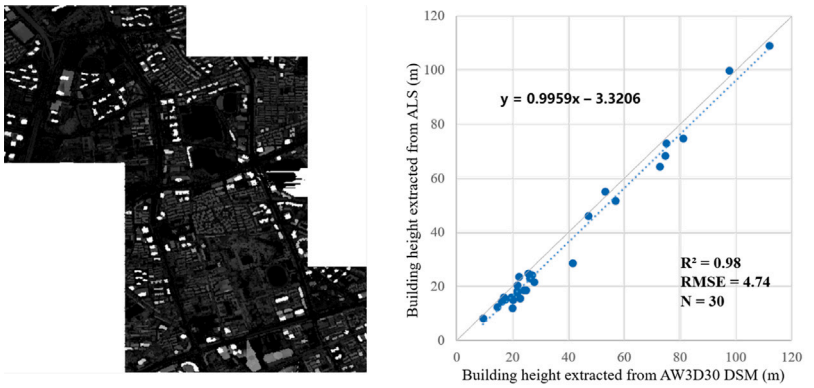

(a) nDSM generated from ALS (b) accuracy of the estimated building height

Fig. 9. Verification of the building height deriving method.

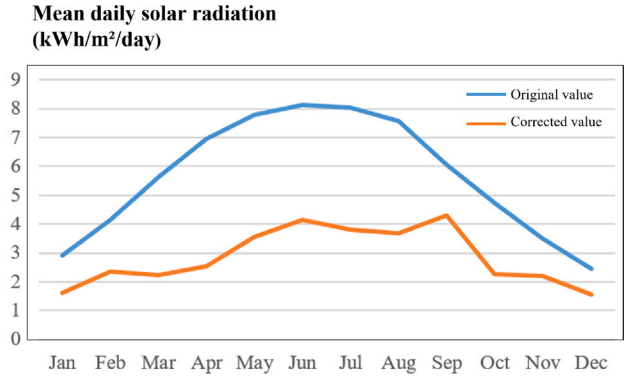

Fig. 10. Corrected values of monthly solar irradiation.

extracted from the AW3D30 DSM can describe the building heights at the city scale, as illustrated in Fig. 8c. In this study, point clouds obtained by Airborne Laser Scanning (ALS) in 2019 are used to generate nDSM which is considered ground truth to verify the accuracy of building heights extracted from AW3D30 DSM (Fig. 9a). We selected 30 buildings that exist in both time phases for verification. The RMSE is computed to assess the performance as follows:

$$RMSE = \sqrt{\frac{\sum_{i=1}^{n}\left(\left(h_A - h_L\right)^2\right.}{n}} \tag{12}$$

where n is the count of sampling points, and h_A and h_L represent the building heights extracted by AW3D30 DSM and ALS, respectively. As presented in Fig. 9, the R^2 and RMSE are 0.98 and 4.74 m, showing a strong correlation and high accuracy. The regression line closely approximates the 1:1 line, but there is a negative offset. This is because AW3D30 DSM was interpolated based on the DSM dataset (5-m mesh version of the World 3D Topographic Data) [38], and pixels representing building heights contain pixels representing ground heights during interpolation. Thus, the building heights may be underestimated slightly. However, since this deviation can be regarded as a systematic error, it does not affect the subsequent analysis of solar PV potential from a 3D perspective.

The AW3D30 DSM data is generated from the PRISM data collected in 2014, while the building footprint extraction is based on GES images from 2019 to 2021. To address this, the potential will be evaluated using the DSM data from the upcoming ALOS-4 satellite, which will replace the ALOS-2 satellite.

5.3. Spatial–temporal distribution of building solar irradiation

As mentioned above, this study utilizes the Å-P formula (Eq. (7)) to correct the negative effect of weather conditions for accurate solar irradiation, whose parameters include the sunshine duration (D_{sun}) and daytime (D_{day}). The total monthly hours D_{sun} and D_{day} listed in Table 2 were collected from China Meteorological Data Center (CMDC).[1] Fig. 10 illustrates the comparison of solar radiance under clear sky conditions and solar radiance corrected by the Å-P formula. The original value under clear sky conditions changes slightly, and the daily average irradiation reaches its highest in June. The main factor affecting this value is the latitude of the region. In practice, this result is overestimated to some extent. The Å-P formula takes into account the negative impact of weather conditions and corrects the original value through the observed sunshine duration hours. Since the result is not only affected by the sun's altitude angle but also affected by climate factors such as rain, haze, etc., the change is larger than the original result.

Fig. 11 shows the final corrected spatial–temporal distribution of solar irradiation in Wuhan in 2021. According to the calculation results, the annual amount of solar irradiation that can be received by the rooftops of buildings in Wuhan in 2021 is 289 737.58 GWh. The average daily solar irradiation intensity is 2.851 kWh/m^2/day. The distribution of solar energy shows obvious seasonal differences. Compared to spring and winter, the amount of solar irradiation is greater in the summer and autumn. The density of building solar potential is higher in urban areas compared to rural areas, and only some regions in rural areas are concentrated, which tends to be consistent with the distribution of building footprints. Table 3 lists the monthly total solar irradiation received by buildings in various districts of Wuhan. Despite the lower density of solar potential on buildings in rural areas, the total amount is significant due to the vast land, thus it is necessary to consider the entire city and not just the urban area when estimating solar potential.

6. Analysis

6.1. Calculation of the solar PV potential on building surfaces

The objective of this study is to assess the solar PV potential on a large scale. Following Hong et al. [24], the solar PV potential on the buildings can be calculated utilizing the solar irradiation and available building area as Eq. (13).

$$Potential_{PV} = k_{PV} \times B_{area} \times SR_{year} \tag{13}$$

[1] http://www.nmic.cn/analysis/yearbooks.html.

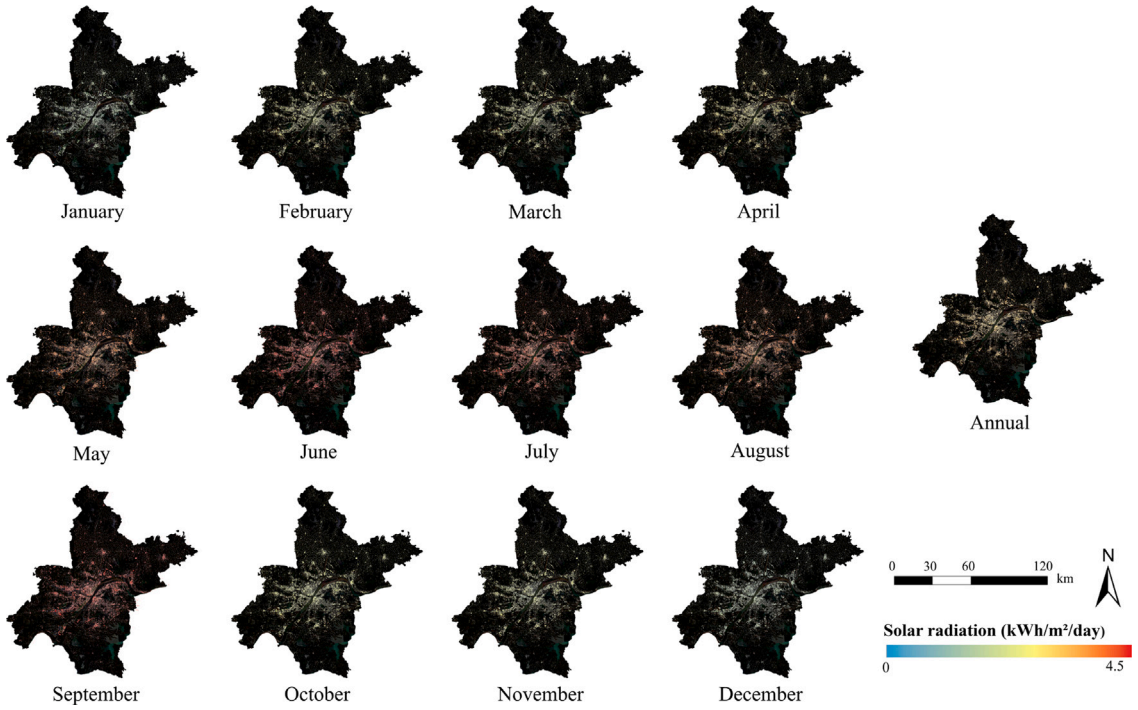

Fig. 11. Spatial–temporal distribution of solar irradiation in Wuhan in 2021.

Table 3
Total building solar irradiation in Wuhan in each month of 2021.

Month	Jan	Feb	Mar	Apr	May	Jun	Jul	Aug	Sep	Oct	Nov	Dec	Total
Huangpi Disrict	674.33	900.00	927.33	1031.48	1494.67	1721.29	1583.38	1549.85	1742.13	947.30	870.99	658.47	56 291.15
Dongxihu District	326.52	435.79	435.79	499.46	723.74	833.48	766.70	750.46	843.57	458.70	421.75	318.84	26 861.31
Xinzhou District	418.45	558.49	558.49	640.08	927.51	1068.14	982.57	961.76	1081.08	587.84	540.49	408.61	34 796.70
Jiangan District	102.39	136.66	136.66	156.63	226.96	261.37	240.43	235.34	264.54	143.84	132.26	99.99	7973.47
Jianghan District	93.61	124.94	124.94	143.19	207.49	238.95	219.81	215.15	241.84	131.50	120.91	91.41	7277.96
Qingshan District	178.95	238.83	238.83	273.72	396.64	456.78	420.18	411.28	462.31	251.38	231.13	174.74	14 324.64
Qiaokou District	86.30	115.19	115.19	132.01	191.30	220.30	202.65	198.36	222.97	121.24	111.47	84.27	6842.44
Wuchang District	155.62	207.70	207.70	238.05	344.94	397.24	365.42	357.68	402.05	218.62	201.01	151.96	12 173.55
Hanyang District	186.32	248.68	248.68	285.01	412.99	475.61	437.50	428.24	481.37	261.75	240.66	181.94	15 067.29
Hongshan District	329.28	439.47	439.47	503.68	729.85	840.52	773.17	756.80	850.69	462.57	425.31	321.54	27 340.79
Caidian District	461.80	616.35	616.35	706.39	1023.60	1178.80	1084.36	1061.39	1193.07	648.74	596.48	450.94	38 676.03
Hannan District	98.40	131.33	131.33	150.51	218.10	251.17	231.04	226.15	254.21	138.23	127.09	96.08	8248.58
Jiangxia District	400.21	534.14	534.14	612.18	887.08	1021.58	939.73	919.83	1033.95	562.22	516.93	390.80	33 863.66
Total	3512.19	4687.57	4714.91	5372.38	7784.87	8965.22	8246.94	8072.27	9073.78	4933.92	4536.47	3429.60	289 737.58

where $Potential_{PV}$ is the potential of solar PV on buildings throughout the year, k_{PV} represents the comprehensive transition efficiency of solar PV systems, B_{area} stands for the area of available buildings, SR_{year} refers to the solar irradiation received by buildings for a year. Considering the technical conditions, k_{PV} is set to 15%. Therefore, the solar PV potential on buildings in Wuhan in 2021 is 43 460.64 GWh. Fig. 12 illustrates the distribution of solar PV potential on buildings. Fig. 12a presents the overall distribution across the entire city. Fig. 12b focuses on districts, showing the solar PV distribution on buildings in the rural district (Dongxihu) and urban districts (Jianghan, Jiangan, Qiaokou, and Hanyang). As can be observed in Fig. 12c and d, the solar PV distribution in rural areas is uniform due to the sparse density of low-rise buildings, which do not block each other. However, in urban areas, due to the high-rise buildings, more areas are affected by shadows. In practice, the installation of solar PV modules can avoid buildings with low solar PV potential due to the shading effect. Additionally, the installation and maintenance of solar PV modules on high-rise buildings can be difficult, making it less convenient. Without quantifying the building heights, it is impossible to identify suitable buildings for PV module installation solely from a 2D perspective.

Hubei Province's 2023 government work report calls for the optimization of energy structures, accelerated transformation of industries towards cleaner practices, and support for the development of renewable energy sources, including solar energy. And subsidies for solar PV power generation in China are facing abolishing elimination altogether [11]. Therefore, an insightful study of the solar PV potential on buildings can assist the local government in promoting the future decarbonization transition. Taking the study area, Wuhan, as an example, the government aims to achieve 370,000 kW installed capacity of PV generation by 2025. Understanding the city-level solar PV potential can enable more optimized site selection and promotion to meet the target.

The proposed method for estimation is entirely based on open-source data. However, these data are limited in supporting more detailed information about buildings, such as determining the aspect and slope of the roof. Besides, the parameters of the Å-P formula for the correction of solar radiation and the comprehensive transition efficiency k_{PV} for the calculation of PV potential are empirical parameters, and therefore inevitably cause some uncertainties. However, for a city-level estimation, the impact of these uncertainties on policy-making and PV planning can be ignored. The follow-up work is to obtain more details of the building from multi-view optical images and SAR images. Moreover, without consideration of comprehensive factors, including grid capacity and economic considerations [11], the potential of solar

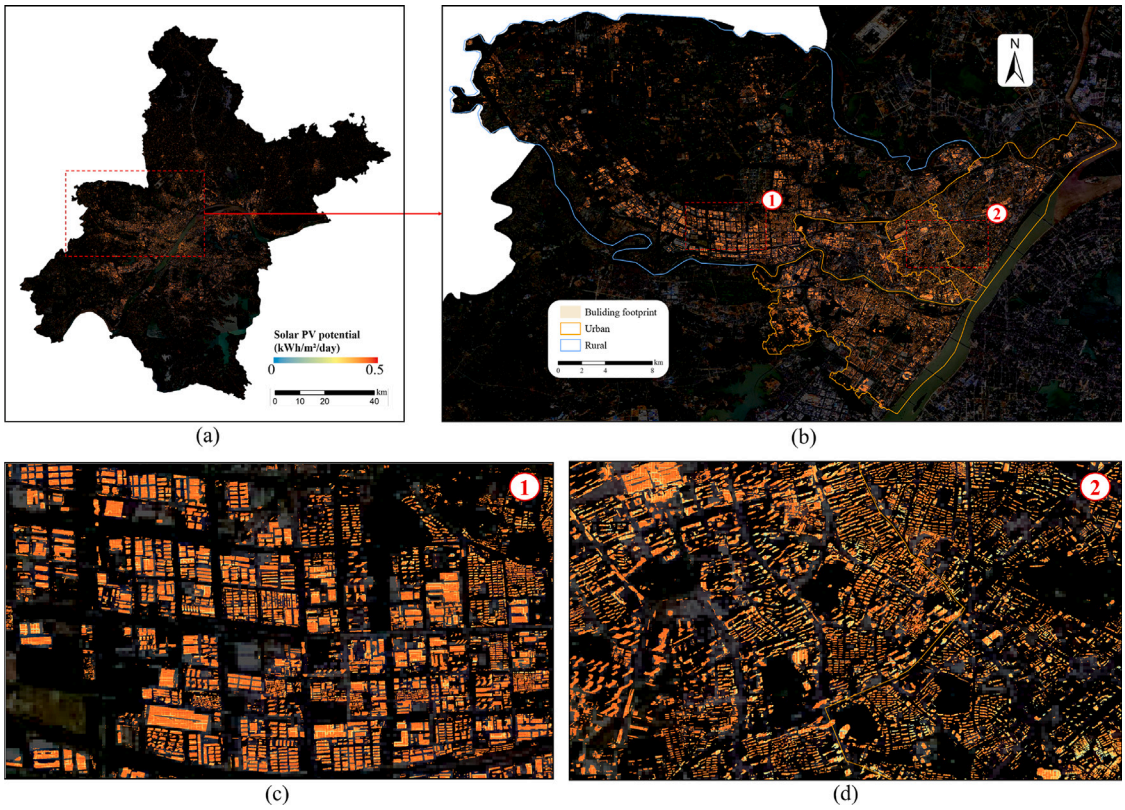

Fig. 12. Distribution of building solar PV potential in 2021. (a) Building solar PV potential in Wuhan. (b) Building solar PV potential in the selected districts. (c) Detailed solar PV potential in rural. (d) Detailed solar PV potential in urban.

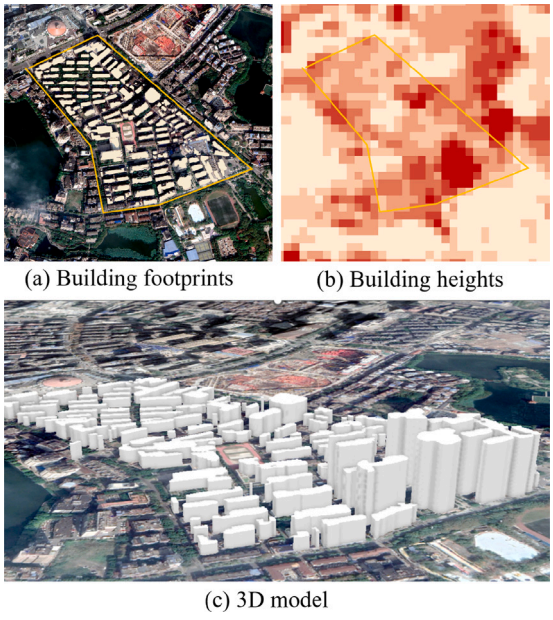

Fig. 13. Diagram of the 3D model of the experimental area.

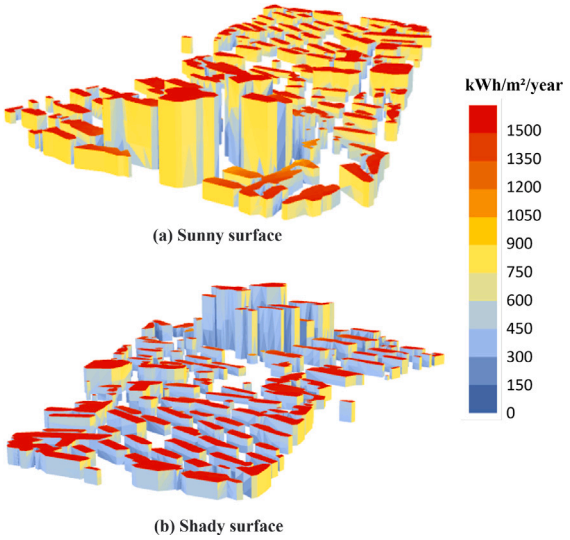

Fig. 14. 3D solar irradiation estimation results.

PV on buildings calculated in this study only represents the theoretical design value, and more factors can be added for subsequent analysis.

In the calculation of building PV potential, only the roof is considered as a feasible location for the placement of solar PV modules. With the advancement of technology, it is now a reality to use PV materials on building facades and windows. Our future research will explore the potential of solar PV on facades and windows at the city scale.

6.2. Estimation of PV potential on building facades

In this study, 3D building information obtained from multi-source RS data can support the estimation of solar PV potential on both facades and rooftops. A study area is selected to demonstrate that the proposed method can provide 3D solar energy estimation for buildings. As shown in Fig. 13, we count the height values of the DSM within each independent polygon of the building footprint and assign the maximum to the polygon as the height of the building. Then, the flat footprint is raised to create a 3D model based on the height. The 3D model is

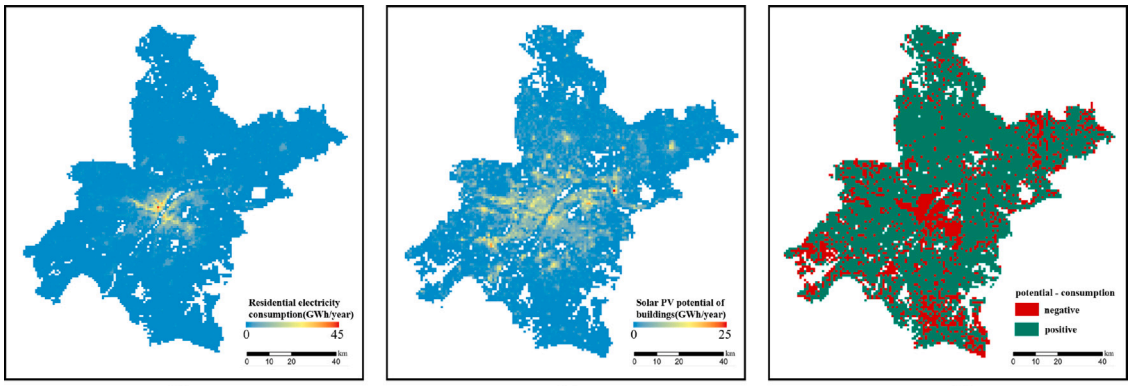

Fig. 15. Comparison of building solar PV potential and residential electricity consumption. (a) Residential electricity consumption in Wuhan. (b) Solar PV potential of buildings in Wuhan. (c) The subtraction between potential and consumption.

Table 4
Comparison of solar irradiation received by rooftops and facades.

Component	Irradiation (kWh/year)	Area (km^2)
Rooftop	95 039	67.86
Facade	138 582	454.57
Total	233 621	522.43

imported into Rhino, and solar irradiation is estimated using the Geco plugin. Since this analysis only demonstrates the potential applicability of the proposed method for 3D solar irradiation estimation, the results are not corrected by the Å-P formula.

The estimation results are shown in Fig. 14. It is evident that building information obtained through multi-source RS data using the proposed method can describe the 3D form of buildings and be applied to estimate the solar irradiation potential of 3D buildings. In terms of the components of the building, rooftops typically receive more solar irradiation per unit area than facades due to their orientation towards the sky and less occlusion caused by surrounding high-rise buildings. Regarding orientation, the sunny facades of the building receive more solar irradiation than the shaded facades. Under clear conditions, the rooftop receives an annual solar irradiation of over 1500 kWh/m^2, while the sunny facade receives generally 750–900 kWh/m^2, and the shady facade receives less than 450 kWh/m^2. Therefore, the shady facade is not an optimal location for installing solar PV modules. As shown in Table 4, in the experiment area, the estimated amount of solar irradiation that the rooftop can receive through a year is 95 039 kWh, and the facades are 138 582 kWh. This is because the area of the facades that can receive solar irradiation is large, so the total amount is higher than on rooftops even at a lower unit receiving efficiency. But considering the cost of installing solar PV modules, the rooftop would be a preferable location compared to the facade. In general, although placing solar PV modules on rooftops yields higher unit revenue compared to facades, the total amount of solar irradiation that the facade of the building can receive is significant, especially for high-rise buildings. To achieve net-zero energy buildings, it is necessary to develop solar PV systems on the facades.

6.3. Analysis of solar PV power supply and demand

In order to verify whether the production capacity of solar PV can meet the electricity consumption needs of residents, the data of LandScan Global 2021[2] is collected, which illustrates the distribution of the population at a resolution of 1 km. According to the China Statistical Yearbook 2021 [54], the average domestic electricity consumption of Chinese residents is 756 kWh. The total amount of electricity consumption can be assessed by multiplying the population by the average electricity consumption per resident. By calculation, the total residential electricity consumption in Wuhan in 2021 amounts to 7751.88 GWh. The estimated solar PV potential on buildings in Wuhan in 2021 reaches 43 460.64 GWh, which is far greater than the consumption. However, due to the problem of power transmission, potential and consumption tend to be considered locally, so we simply assume that an off-grid power system is used to store and consume the electricity generated by solar PV nearby. In this system, the application of the Electric Energy Storage System (EESS) needs to be considered because production and consumption are not always contemporary. Solar PV generation occurs during the day, while peak electricity demand typically happens at night. Therefore, EESS is essential for fully exploiting solar PV energy. The distribution of residential electricity consumption in Wuhan in 2021 is shown in Fig. 15a, with a resolution of 1 km. The potential of solar PV on buildings is resampled to the same resolution for comparison purposes. (Fig. 15b). The distribution of residential electricity consumption is concentrated, while the supply potential of solar PV, on the contrary, is relatively dispersed. This is because the population is mainly concentrated in the central area, while the population density in the surrounding area is low. In rural areas, the buildings are mostly low-rise, which can support large areas for obtaining solar irradiation. By pixel-by-pixel subtracting the potential of solar PV on buildings and the residents' electricity consumption, the supply and demand can be analyzed from the local scale.

Based on Fig. 15c, the solar PV potential in most areas is sufficient to meet the needs of residents, but there will be insufficient situations in areas with high population density. The power sector can plan the placement of PV modules and allocate power transmission according to supply and demand.

7. Conclusions

This study proposes an approach for assessing the city-scale potential of solar PV on buildings using multi-source open RS data without additional labor costs. The building footprints are extracted using publicly available GES images based on UDA, and the coarse LULC product is introduced to provide prior knowledge to reduce negative transfer. In order to obtain the 3D information of buildings for supporting occlusion analysis, AW3D30 DSM is used to extract the height of buildings in the city. After obtaining the 3D information of the buildings, the potential of solar PV is estimated. The amount of solar irradiation received by buildings in Wuhan in 2021 is 289 737.58 GWh, and the potential of solar PV calculated on this basis is 43 460.64 GWh. The calculation results of this study can provide detailed solar PV potential distribution, which can help in the selection of optimal sites and planning for the

[2] https://landscan.ornl.gov/.

installation of PV modules. The framework proposed in this study does not require data acquisition costs or labor costs for sample labeling used in deep learning, thus, it demonstrates strong scalability and has the potential to be applied globally.

Due to data limitations, it is difficult to obtain the details of building roofs, such as slope and aspect, which can affect the amount of solar irradiation received and the installation of solar PV modules. Other sources of data, such as SAR images, are being considered for extracting this part of the information to provide more refined estimation results. In addition, solar PV materials can currently be installed on facades and windows. The estimation on facades has been conducted in a small area, and we will incorporate this into the city-scale framework in future work.

CRediT authorship contribution statement

Zhe Chen: Writing – original draft, Visualization, Validation, Supervision, Project administration, Methodology, Investigation, Data curation, Conceptualization. **Bisheng Yang:** Writing – review & editing, Supervision, Resources, Investigation, Funding acquisition, Conceptualization. **Rui Zhu:** Writing – review & editing, Supervision. **Zhen Dong:** Writing – review & editing, Supervision, Methodology, Funding acquisition, Conceptualization.

Declaration of competing interest

The authors declare that they have no known competing financial interests or personal relationships that could have appeared to influence the work reported in this paper.

Data availability

Data will be made available on request.

Acknowledgments

This research is supported by the National Natural Science Foundation Project (No. 42130105) and Key Laboratory of Spatial–temporal Big Data Analysis and Application of Natural Resources in Megacities, MNR (No. KFKT-2022-01).

Appendix. Abbreviations and symbols

Please see Table A.1.

Table A.1
Abbreviations and symbols.

Abbreviations		Symbols	
RS	Remote Sensing	I	The remote sensing image
PV	Photovoltaic	M	The mask obtained by artificial surface
UDA	Unsupervised Domain Adaptation	Ind_{as}	The index of the artificial surface
DSSN	Deep Semantic Segmentation Network	G	The segmentaction network
DSM	Digital Surface Model	D	The fine-grained discriminator
BiPVs	Building-integrated Photovoltaics	L_{seg}	The cross-entropy loss for segmentation
LiDAR	Light Detection and Ranging	λ_{adv}	The parameter for balancing losses
GES	Google Earth Satellite	L_{adv}	The adversarial loss for domain adaptation
GIS	Geographic Information System	Y	The labels from the source domain
ECMWF	European Centre for Medium Range Weather Forecasts	y	The one-hot label entry for the pixel
UAV	Unmanned Aerial Vehicle	P	The class probability predicted by G
TLS	Terrestrial Laser Scanning	L_D	The discriminator loss for domain adaptation
SVM	Support Vector Machine	e	The domain encodings used in domain adaptation
VHR	Very High Resolution	s	The size of sliding window in deriving building heights
GSV	Google Street View	k	The parameter for choosing ground point candidates
OSM	OpenStreetMap	$Global_R$	The global solar irradiation
AOI	Areas of Interest	$Direct_R$	The direct component of solar irradiation
LULC	Land Use and Land Cover	$Diffuse_R$	The diffuse component of solar irradiation
PRISM	Panchromatic Remote-sensing Instrument for Stereo Mapping	$Global_{corr}$	The global solar irradiation corrected by the actual weather
ALOS	Advanced Land Observing Satellite	a	The parameter for the Å-P formula
SRTM	Shuttle Radar Topography Mission	b	The parameter for the Å-P formula
GDEM	Global Digital Elevation Model	D_{sun}	The daily sunshine duration for the Å-P formula
RU	Resolution Uniform	D_{day}	The daily daytime for the Å-P formula
DNT	Digital Number Transfer	h_A	The building heights extracted by AW3D30 DSM
MSF	Multi-Scale Feature Aggregation	h_L	The building heights extracted by ALS
MST	Multi-Scale Testing	$Potential_{PV}$	The potential of solar PV on buildings
DEM	Digital Elevation Model	k_{PV}	The comprehensive transition efficiency of solar PV systems

(*continued on next page*)

Table A.1 (*continued*).

Abbreviations		Symbols	
nDSM	normalized Digital Surface Model	B_{area}	The area of available buildings
ALS	Airborne Laser Scanning	SR_{year}	The solar irradiation received by buildings
CMDC	China Meteorological Data Center		
CSY	China Statistical Yearbook		
EESS	Electric Energy Storage System		

References

[1] Sun Y, Li Y, Yu T, Zhang X, Liu L, Zhang P. Resource extraction, environmental pollution and economic development: Evidence from prefecture-level cities in China. Resour Policy 2021;74:102330.

[2] Savaresi A. The Paris Agreement: a new beginning? J Energy Nat Resour Law 2016;34(1):16–26.

[3] Duan H-B, Zhang G-P, Zhu L, Fan Y, Wang S-Y. How will diffusion of PV solar contribute to China's emissions-peaking and climate responses? Renew Sustain Energy Rev 2016;53:1076–85.

[4] Cozzi L, Gould T, Bouckart S, Crow D, Kim T, Mcglade C, Olejarnik P, Wanner B, Wetzel D. World energy outlook 2020. Paris, France: International Energy Agency; 2020, p. 1–461.

[5] NEA. Statistics of the national power industry in 2020. 2021, http://www.nea.gov.cn/2021-01/20/c_139683739.htm, [accessed 14 Dec 2022].

[6] Xie H, Zhang C, Hao B, Liu S, Zou K. Review of solar obligations in China. Renew Sustain Energy Rev 2012;16(1):113–22.

[7] Sánchez-Aparicio M, Martín-Jiménez J, Del Pozo S, González-González E, Lagüela S. Ener3DMap-SolarWeb roofs: A geospatial web-based platform to compute photovoltaic potential. Renew Sustain Energy Rev 2021;135:110203.

[8] Aslani M, Seipel S. Automatic identification of utilizable rooftop areas in digital surface models for photovoltaics potential assessment. Appl Energy 2022;306:118033.

[9] Brito M, Freitas S, Guimarães S, Catita C, Redweik P. The importance of facades for the solar PV potential of a Mediterranean city using LiDAR data. Renew Energy 2017;111:85–94.

[10] Sharma P, Kolhe M, Sharma A. Economic performance assessment of building integrated photovoltaic system with battery energy storage under grid constraints. Renew Energy 2020;145:1901–9.

[11] Zhong T, Zhang Z, Chen M, Zhang K, Zhou Z, Zhu R, Wang Y, Lü G, Yan J. A city-scale estimation of rooftop solar photovoltaic potential based on deep learning. Appl Energy 2021;298:117132.

[12] Wiginton L, Nguyen HT, Pearce JM. Quantifying rooftop solar photovoltaic potential for regional renewable energy policy. Comput Environ Urban Syst 2010;34(4):345–57.

[13] Li Y, Ding D, Liu C, Wang C. A pixel-based approach to estimation of solar energy potential on building roofs. Energy Build 2016;129:563–73.

[14] Cheng L, Zhang F, Li S, Mao J, Xu H, Ju W, Liu X, Wu J, Min K, Zhang X, et al. Solar energy potential of urban buildings in 10 cities of China. Energy 2020;196:117038.

[15] Li Q, Taubenböck H, Shi Y, Auer S, Roschlaub R, Glock C, Kruspe A, Zhu XX. Identification of undocumented buildings in cadastral data using remote sensing: Construction period, morphology, and landscape. Int J Appl Earth Obs Geoinf 2022;112:102909.

[16] Lingfors D, Bright JM, Engerer NA, Ahlberg J, Killinger S, Widén J. Comparing the capability of low-and high-resolution LiDAR data with application to solar resource assessment, roof type classification and shading analysis. Appl Energy 2017;205:1216–30.

[17] Chen Z, Yu B, Li Y, Wu Q, Wu B, Huang Y, Wu S, Yu S, Mao W, Zhao F, et al. Assessing the potential and utilization of solar energy at the building-scale in Shanghai. Sustainable Cities Soc 2022;82:103917.

[18] Vo AV, Laefer DF, Smolic A, Zolanvari SI. Per-point processing for detailed urban solar estimation with aerial laser scanning and distributed computing. ISPRS J Photogramm Remote Sens 2019;155:119–35.

[19] Lee S, Iyengar S, Feng M, Shenoy P, Maji S. Deeproof: A data-driven approach for solar potential estimation using rooftop imagery. In: Proceedings of the 25th ACM SIGKDD international conference on knowledge discovery & data mining. 2019, p. 2105–13.

[20] Krapf S, Kemmerzell N, Khawaja Haseeb Uddin S, Hack Vázquez M, Netzler F, Lienkamp M. Towards scalable economic photovoltaic potential analysis using aerial images and deep learning. Energies 2021;14(13):3800.

[21] Yan L, Zhu R, Kwan M-P, Luo W, Wang D, Zhang S, Wong MS, You L, Yang B, Chen B, et al. Estimation of urban-scale photovoltaic potential: A deep learning-based approach for constructing three-dimensional building models from optical remote sensing imagery imagery. Sustainable Cities Soc 2023;104515.

[22] Reichstein M, Camps-Valls G, Stevens B, Jung M, Denzler J, Carvalhais N. Deep learning and process understanding for data-driven Earth system science. Nature 2019;566(7743):195–204.

[23] Izquierdo S, Rodrigues M, Fueyo N. A method for estimating the geographical distribution of the available roof surface area for large-scale photovoltaic energy-potential evaluations. Sol Energy 2008;82(10):929–39.

[24] Hong T, Lee M, Koo C, Jeong K, Kim J. Development of a method for estimating the rooftop solar photovoltaic (PV) potential by analyzing the available rooftop area using Hillshade analysis. Appl Energy 2017;194:320–32.

[25] Assouline D, Mohajeri N, Scartezzini J-L. Large-scale rooftop solar photovoltaic technical potential estimation using Random Forests. Appl Energy 2018;217:189–211.

[26] Zhang Y, Ren J, Pu Y, Wang P. Solar energy potential assessment: A framework to integrate geographic, technological, and economic indices for a potential analysis. Renew Energy 2020;149:577–86.

[27] Kodysh JB, Omitaomu OA, Bhaduri BL, Neish BS. Methodology for estimating solar potential on multiple building rooftops for photovoltaic systems. Sustainable Cities Soc 2013;8:31–41.

[28] Fu P, Rich PM. A geometric solar radiation model with applications in agriculture and forestry. Comput Electron Agric 2002;37(1–3):25–35.

[29] Huang Y, Chen Z, Wu B, Chen L, Mao W, Zhao F, Wu J, Wu J, Yu B. Estimating roof solar energy potential in the downtown area using a GPU-accelerated solar radiation model and airborne LiDAR data. Remote Sens 2015;7(12):17212–33.

[30] Suomalainen K, Wang V, Sharp B. Rooftop solar potential based on LiDAR data: Bottom-up assessment at neighbourhood level. Renew Energy 2017;111:463–75.

[31] Liang F, Yang B. Multilevel solar potential analysis of building based on ubiquitous point clouds. In: 2018 26th International conference on geoinformatics. IEEE; 2018, p. 1–4.

[32] Mohajeri N, Assouline D, Guiboud B, Bill A, Gudmundsson A, Scartezzini J-L. A city-scale roof shape classification using machine learning for solar energy applications. Renew Energy 2018;121:81–93.

[33] Wu B, Wu S, Li Y, Wu J, Huang Y, Chen Z, Yu B. Automatic building rooftop extraction using a digital surface model derived from aerial stereo images. J Spatial Sci 2020;67(1):21–40.

[34] Li Q, Krapf S, Shi Y, Zhu XX. SolarNet: A convolutional neural network-based framework for rooftop solar potential estimation from aerial imagery. Int J Appl Earth Obs Geoinf 2023;116:103098.

[35] Li X, Ratti C. Mapping the spatio-temporal distribution of solar radiation within street canyons of Boston using Google Street View panoramas and building height model. Landsc Urban Plan 2019;191:103387.

[36] Van Etten A, Lindenbaum D, Bacastow TM. Spacenet: A remote sensing dataset and challenge series. 2018, arXiv preprint arXiv:1807.01232.

[37] Jun C, Ban Y, Li S. Open access to Earth land-cover map. Nature 2014;514(7523):434.

[38] Tadono T, Nagai H, Ishida H, Oda F, Naito S, Minakawa K, Iwamoto H. Generation of the 30 M-mesh global digital surface model by ALOS PRISM. Int Arch Photogramm, Remote Sens Spatial Inf Sci 2016;41.

[39] Grohmann CH. Evaluation of TanDEM-X DEMs on selected Brazilian sites: Comparison with SRTM, ASTER GDEM and ALOS AW3D30. Remote Sens Environ 2018;212:121–33.

[40] Li H, Zhao J. Evaluation of the newly released worldwide AW3D30 DEM over typical landforms of China using two global DEMs and ICESat/GLAS data. IEEE J Sel Top Appl Earth Obs Remote Sens 2018;11(11):4430–40.

[41] Tan C, Sun F, Kong T, Zhang W, Yang C, Liu C. A survey on deep transfer learning. In: International conference on artificial neural networks. Springer; 2018, p. 270–9.

[42] Wang J, Zheng Z, Ma A, Lu X, Zhong Y. LoveDA: A remote sensing land-cover dataset for domain adaptive semantic segmentation. 2021, arXiv preprint arXiv:2110.08733.

[43] Zou Y, Yu Z, Kumar B, Wang J. Unsupervised domain adaptation for semantic segmentation via class-balanced self-training. In: Proceedings of the European conference on computer vision. ECCV, 2018, p. 289–305.

[44] Zhang P, Zhang B, Zhang T, Chen D, Wang Y, Wen F. Prototypical pseudo label denoising and target structure learning for domain adaptive semantic segmentation. In: Proceedings of the IEEE/CVF conference on computer vision and pattern recognition. 2021, p. 12414–24.

[45] Araslanov N, Roth S. Self-supervised augmentation consistency for adapting semantic segmentation. In: Proceedings of the IEEE/CVF conference on computer vision and pattern recognition. 2021, p. 15384–94.

[46] Chen Z, Yang B, Ma A, Peng M, Li H, Chen T, Chen C, Dong Z. Joint alignment of the distribution in input and feature space for cross-domain aerial image semantic segmentation. Int J Appl Earth Obs Geoinf 2022;115:103107.

[47] Zhang S, Wen L, Bian X, Lei Z, Li SZ. Single-shot refinement neural network for object detection. In: CVPR. 2018.
[48] Wang J, Ma A, Zhong Y, Zheng Z, Zhang L. Cross-sensor domain adaptation for high spatial resolution urban land-cover mapping: From airborne to spaceborne imagery. Remote Sens Environ 2022;277:113058.
[49] Huang H, Chen P, Xu X, Liu C, Wang J, Liu C, Clinton N, Gong P. Estimating building height in China from ALOS AW3D30. ISPRS J Photogramm Remote Sens 2022;185:146–57.
[50] Niimura T, Sakamoto N, Ozawa K. Estimating hourly profiles of insolation based on weekly weather forecast. Int J Energy Power Eng 2014;3(6–2):1–6.
[51] Meeus J. Astronomical algorithms. Richmond; 1991.
[52] Paulescu M, Stefu N, Calinoiu D, Paulescu E, Pop N, Boata R, Mares O. Ångström–Prescott equation: Physical basis, empirical models and sensitivity analysis. Renew Sustain Energy Rev 2016;62:495–506.
[53] Luo Y, Zheng L, Guan T, Yu J, Yang Y. Taking a closer look at domain shift: Category-level adversaries for semantics consistent domain adaptation. In: Proceedings of the IEEE/CVF conference on computer vision and pattern recognition. 2019, p. 2507–16.
[54] CSY. China statistical yearbook 2021. 2022, http://www.stats.gov.cn/sj/ndsj/2021/indexch.htm, [accessed 23 Dec 2022].